

Engineering inverse woodpile and woodpile photonic crystal solar cells for light trapping

Baomin Wang¹, Kevin P Chen² and Paul W Leu¹

¹Department of Industrial Engineering, University of Pittsburgh, Pittsburgh, PA 15261, USA

²Department of Electrical Engineering, University of Pittsburgh, Pittsburgh, PA 15261, USA

E-mail: pleu@pitt.edu

Received 25 January 2016, revised 18 March 2016


Accepted for publication 5 April 2016

Published 25 April 2016



Abstract

We demonstrate that inverse woodpile and woodpile photonic crystal nanocrystalline silicon structures may be engineered for light trapping in solar cells. We use finite-difference time-domain simulations to show that the geometry of these photonic crystals may be varied such that absorption in the infrared, visible, and ultraviolet parts of the spectrum may all be improved. The short-circuit current density and ultimate efficiency are also improved. We found a 77.1% and 106% absorption enhancement in the optimized inverse woodpile and woodpile structures respectively, compared to a nanocrystalline silicon thin film of the equivalent thickness. The inverse woodpile structures may be approximated as a thin film with effective index of refraction, whereas the woodpile structures exhibit resonances from the coupling of TE and TM leaky modes in the stacked cylinders. Woodpile photonic crystal structures exhibit improved performance compared to inverse woodpile structures over a range of equivalent thicknesses and incidence angles. The performance of woodpile structures is also generally insensitive to the diameter, pitch and number of layers, whereas inverse woodpile structures are much more sensitive to morphology.

 Online supplementary data available from stacks.iop.org/nano/27/225404/mmedia

Keywords: woodpile, photonic crystal, solar cells, silicon

(Some figures may appear in colour only in the online journal)

1. Introduction

There has been much research interest in thin-film solar cells, which offer the potential for module cost reduction through the utilization of less material and the relaxation of material purity requirements. Light trapping is of great importance for thin-film solar cells in order to increase the optical absorption in the photoactive region and allow for moderate efficiencies with less material. Many wave optics light-trapping schemes, which involve structures with length scales comparable to or less than the wavelengths of most of the solar spectrum, have been investigated for increasing the absorption in silicon thin-film photovoltaics. For example, diffraction gratings [1], nanowires [2–6], and nanocones [7, 8] have been studied extensively for this purpose.

Ultrathin films with thicknesses below 1000 nm may enable flexible solar cells while further reducing the amount

of material used and lowering purity requirements. Ultrathin film silicon (Si) has been demonstrated to be mechanically flexible and is able to be incorporated into flexible, light-weight polymer substrates for solar cells [9]. The challenge in these ultrathin structures is that Si is an indirect band gap material and thus photons with energy just above the Si band gap require phonon interactions for absorption. Si has an absorption length greater than 1000 nm for photons with wavelength $\lambda > 550$ nm. 86% of photons have $\lambda > 550$ nm in the AM1.5G solar spectrum [10].

Various simulation studies have demonstrated how ultrathin Si may be structured to improve solar absorption. For example, a crystalline Si double-layer photonic crystal with the equivalent thickness of a 222 nm film was shown to have a maximum photocurrent density of 16.9 mA cm^{-2} [11]. A 100 nm thick crystalline Si film with plasmonic hemisphere arrays on top [12] has been shown to have a maximum short-

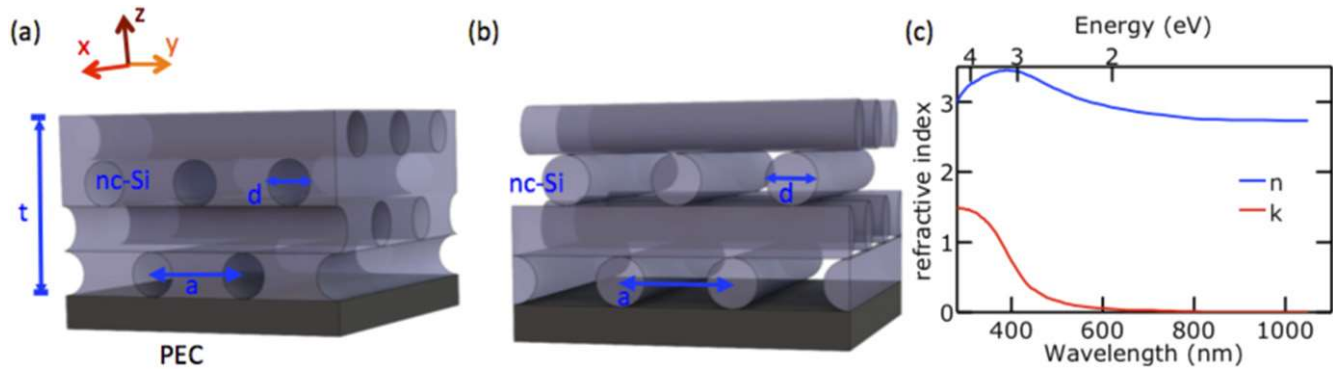


Figure 1. Schematic of the (a) inverse woodpile photonic crystal structure and (b) woodpile photonic crystal structure. (c) Optical constants of nanocrystalline silicon.

circuit current density of 6.1 mA cm^{-2} compared to 5.0 mA cm^{-2} without the hemispheres. In addition, a 50 nm crystalline Si ultrathin film with a plasmonic grating (0.96 mA cm^{-2}) has also demonstrated 43% enhancement compared to without the grating (0.67 mA cm^{-2}) [13].

Photonic crystals [11, 14–16] which allow for the engineering of the photonic density of states, may be utilized for light trapping in the active region of the solar cell. Recently, the author Chen's group has demonstrated the ability to fabricate photonic crystal templates through interference lithography and one or two laser exposures, akin to traditional photolithography processes [17–19]. These templates may be used to form inverse woodpile (IWP) or woodpile (WP) photonic crystals by infiltrating the polymer with nanocrystalline silicon (nc-Si) which has a similar band gap and higher effective absorption coefficient compared to crystalline Si [20].

In this paper, we present detailed numerical electrodynamic investigations of IWP and WP photonic crystal nc-Si solar cells for a variety of geometries and compare them to thin-film structures. We analyze the achievable absorption enhancement across the solar spectrum and find these structures exhibit improved light trapping over thin-film structures. The absorption resonances in the IWP and WP photonic crystals may be approximated by a thin film with an effective index of refraction and stacked cylinders, respectively. We further analyze the two structures across a range of equivalent thicknesses and incidence angles.

2. Results and discussion

Figure 1 shows the schematics of the (a) IWP and (b) WP photonic crystal structures studied. The active layer consists of nc-Si placed on top of a perfect electric conductor (PEC). The IWP photonic crystal is formed by stacking N layers of air cylinders in nc-Si, where each layer is rotated by 90° from the layer below. N is constrained to be an integer. The stacking pattern is a four-layer sequence where the third and fourth layers have the same orientation as the first and second layers, respectively, but are offset by half of the horizontal lattice constant. The WP photonic crystal has the same

stacking pattern, but consists of a lattice of nc-Si cylinders surrounded by air.

The parameters of the structures are the horizontal period a of the lattice, the diameter d of the cylinders, and the total thickness t . $t = Nd$. The diameters of the cylinders are smaller than or equal to the horizontal lattice period, $d \leq a$. The thickness L of a thin film with the same amount of nc-Si (or equivalent thickness) as the IWP and WP structures are

$$L = Nd - \frac{N \pi d^2}{a} \quad (1)$$

and

$$L = \frac{N \pi d^2}{a} \quad (2)$$

respectively.

We employed the finite-difference time-domain method for solving Maxwell's equations. The optical constants of the nc-Si used in this work are shown in figure 1(c) [21]. The solar absorption, ultimate efficiency, and short-circuit current density were evaluated under the global 37° tilt Air Mass 1.5 spectrum³ using the same formulas as those previously used [22]. The ultimate efficiency describes the cell efficiency when each photon absorbed produces one electron–hole pair, and these photoexcited carriers are collected without recombination such as when the temperature of the cell is 0 K. The short-circuit current is calculated under the same assumptions. The band gap of nc-Si is $E_g = 1.12 \text{ eV}$.

We evaluated the optical properties of the IWP and WP structures over the energy range of the solar spectrum from 1.12 to 4.4 eV (wavelengths from 1100 to 280 nm). A uniform mesh of $10 \times 10 \times 10 \text{ nm}$ was utilized where the ultimate efficiency was found to have converged within 1%. Perfectly matched layer and PEC boundary conditions were used for the upper and lower boundary of the simulation cell, respectively [23]. Appropriate boundary conditions were used for the side boundaries to model the periodic nature of the arrays. The optical spectra of the photonic crystals were averaged for light polarized in the x - and y -directions.

³ Solar spectral irradiance: air mass 1.5 <http://redc.nrel.gov/solar/spectra/am1.5/>

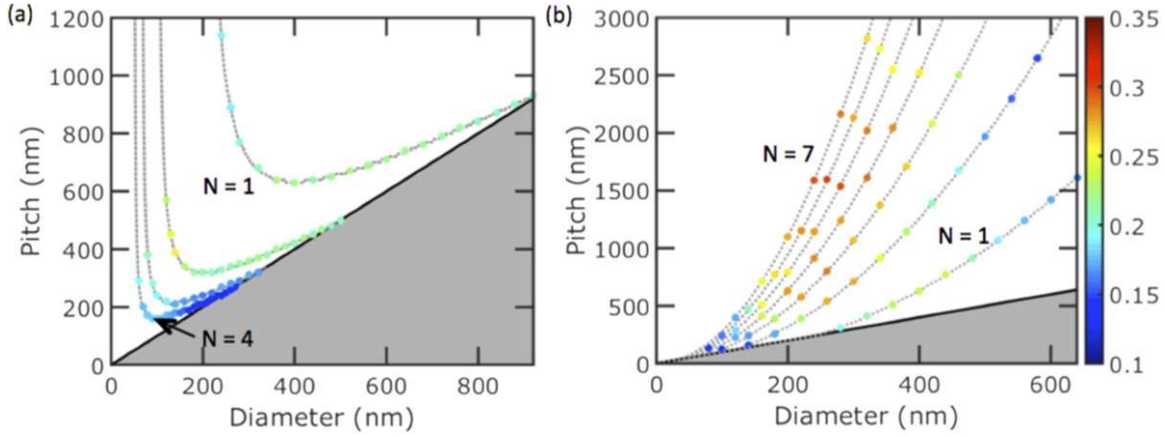


Figure 2. Scatter plots of ultimate efficiency for different (a) IWP and (b) WP structures subject to the constraint that $L = 200$ nm and $d < a$.

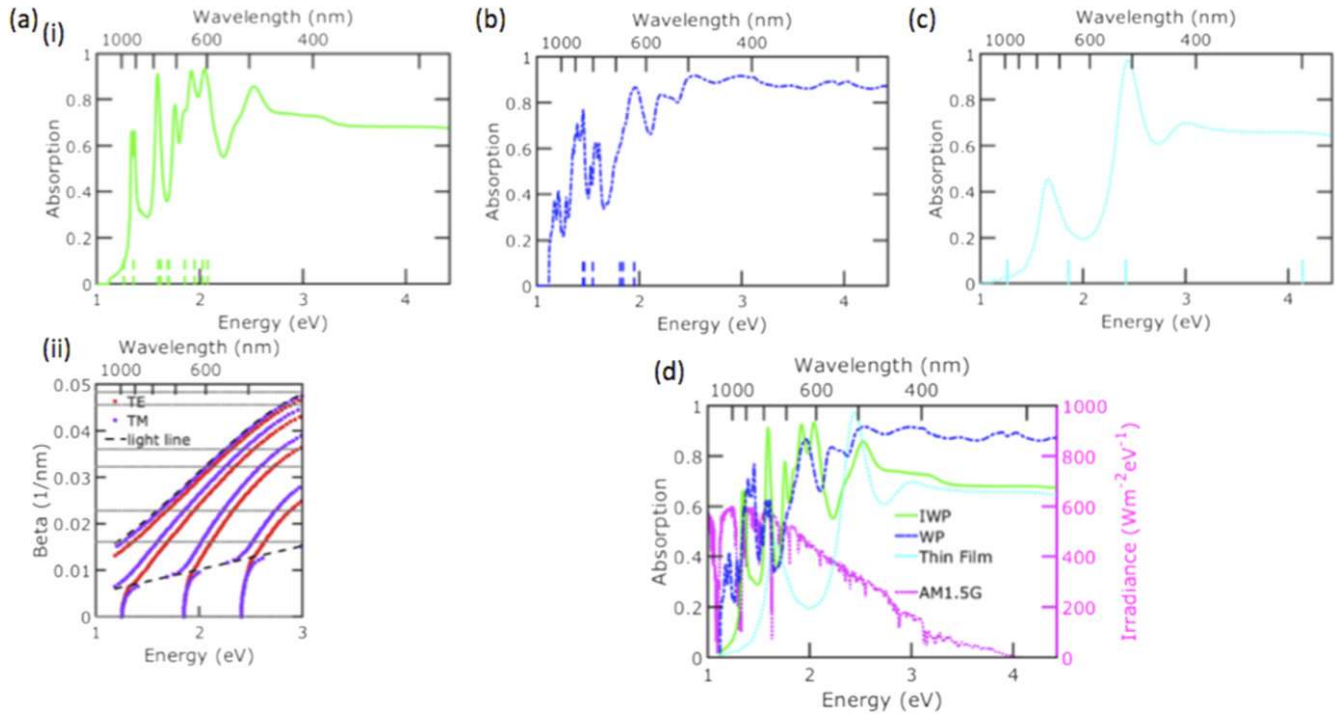


Figure 3. Absorption spectra of three different nc-Si structures: (a) IWP with $N = 2$, $a = 390$ nm, and $d = 140$ nm, (b) WP with $N = 6$, $a = 1600$ nm, and $d = 260$ nm, and (c) thin film with $L = 200$ nm. The dispersion relation of the leaky or quasi-guided modes of a thin film with volumetric averaged index of refraction is shown in (a)(ii). (d) The three absorption spectra are plotted together with the irradiance of the Air Mass 1.5 global solar spectrum shown on the right y-axis.

For this study, we first focused on the equivalent thickness $L = 200$ nm and optimized the number of layers N , pitch a , and diameter d of the IWP and WP structures for the maximum solar absorption or equivalently, the maximum ultimate efficiency. The constraint of comparing structures with the same equivalent thickness (as defined by equations (1) and (2) for the IWP and WP structures, respectively) results in a series of contour lines as shown in figure 2. The ultimate efficiency of the simulated structures is plotted on these contour lines for various number of layers N , diameters d , pitches a . The region of the parameter space that does not satisfy the constraint $d \leq a$ is shaded gray. Figure 2(a) shows the results for the IWP structure for $N = 1$

to 4. The optimal IWP structure is $N = 2$, $a = 390$ nm, and $d = 140$ nm where the ultimate efficiency is 25.8%. Figure 2(b) shows the results for the WP structure, where the optimal structure is $N = 6$, $a = 1600$ nm, and $d = 260$ nm, where the ultimate efficiency is 30.1%. The IWP structure is very sensitive to the number of layers and morphology, whereas the WP structure has a broad range of layers and morphologies which perform close to the optimum. The WP structures have ultimate efficiencies $> 27.0\%$ for $N = 2$ to 7 with a broad range of pitches and diameters. The ultimate efficiency is not very strongly dependent on pitch when the pitch is large, because the cylinders are far from each other horizontally.

Figure 3 plots the absorption spectra as a function of energy, $A(E)$, for the (a) optimal IWP structure, (b) optimal WP structure, and (c) 200 nm nc-Si thin film. The absorption spectra were calculated by $A(E) = 1 - R(E)$. We demonstrate that the IWP structure may be approximated as a thin-film waveguide of thickness $t = Nd = 280$ nm on metal with an effective index of refraction. The absorption resonances of the IWP structure closely match those of a waveguide with a volumetric averaged index of refraction. Photonic crystals consisting of a double layer of holes [11] and square patterns [24] have similarly been shown that they may be approximated as an effective homogeneous layer waveguide for a thin film on metal, so that the leaky TE modes satisfy

$$k_{2x} \cot(k_{2x}t) = ik_{1x} \quad (3)$$

and the leaky TM modes satisfy

$$ik_{2x} \tan(k_{2x}t) = n_2^2 k_{1x} \quad (4)$$

where $k_{1x} = [k_0^2 - \beta^2]^{1/2}$ and $k_{2x} = [(n_2 k_0)^2 - \beta^2]^{1/2}$. k_{1x} is the transverse component of the wavevector outside the semiconductor, while k_{2x} is the transverse part of the wavevector inside the semiconductor. n_2 is the effective index of refraction of the nanocrystalline silicon based on its volumetric fill factor. k_0 is the free-space wave number. The dispersion relation of various TE and TM leaky (or quasi-guided) modes are shown in figure 3(a)(ii). The light lines for the air and the effective index of refraction material are also shown. The horizontal gray dashed lines correspond to the magnitude of the reciprocal lattice vectors of the photonic crystal square lattice

$$k = \sqrt{\left(\frac{2\pi m}{a}\right)^2 + \left(\frac{2\pi p}{a}\right)^2} \quad (5)$$

where m and p are integers. When the wavevector of a leaky mode β is equal to the reciprocal lattice vector, normally incident light can couple into the leaky mode and there is an absorption peak. The photon energies where this occurs for energies below 2.1 eV are shown with the green dashed lines at the bottom of figure 3(a)(i).

In contrast, for the WP photonic crystal, the absorption peaks are related to the leaky resonant modes in a cylinder and poorly approximated by that of an effective index homogeneous layer. The leaky TE modes may be calculated from

$$\frac{J'_m(n_2 k_0 d/2)}{n_2 J_m(n_2 k_0 d/2)} = \frac{H'_m(k_0 d/2)}{H_m(k_0 d/2)} \quad (6)$$

and the leaky TM modes may be calculated from

$$n_2 \frac{J'_m(n_2 k_0 d/2)}{J_m(n_2 k_0 d/2)} = \frac{H'_m(k_0 d/2)}{H_m(k_0 d/2)} \quad (7)$$

where J_m and H_m are the m th order Bessel and Hankel functions of the first kind, respectively [25]. The prime denotes differentiation with respect to the arguments. The location of the TE and TM modes below 2.1 eV are shown with blue dashed lines at the bottom of figure 3(b). The lowest energy modes are the TE₁₁ and TM₀₁ modes at 1.45 and 1.54 eV, respectively. These modes couple to one another

Table 1. % of absorption in different regions of the solar spectrum. The infrared and total solar regions are calculated only for energies above the nc-Si band gap ($E > 1.12$ eV).

Structure	IR	Vis	UV	Total
IWP	30.1	72.5	69.9	52.6
IWP	44.6	75.3	88.0	61.3
Thin Film	11.3	66.9	44.5	29.7

Table 2. The total solar absorption, A_{sol} (%), short-circuit current density J_{sc} (mA cm^{-2}), and the ultimate efficiency η (%).

Structure	A_{sol}	J_{sc}	η
IWP	33.4	23.1	25.8
WP	39.0	26.9	30.1
Thin Film	18.8	13.0	14.6

since the n-Si cylinders are stacked on top of one another, resulting in resonance modes that are closer to the band gap. This mode coupling is also mostly independent of pitch, since this is a horizontal pitch, as long as the cylinders are not that close to one another. The absorption spectrum and ultimate efficiency are also largely independent of pitch, as shown in figure 2(b). Figure 3(c) plots the absorption spectrum for the 200 nm thick c-Si thin film. The absorption peaks are Fabry–Perot TEM modes which satisfy equations (3) and (4) when $\beta = 0$. The locations of the TEM are shown with cyan dashed lines at the bottom of figure 3(c). The numerically simulated resonances correspond well to the analytical solution, but are slightly red-shifted due to numerical error. Figure 3(d) plots all the absorption spectra together for comparison. The irradiance of the Air Mass 1.5 global solar spectrum is shown in the right y-axis.

Table 1 lists the fraction of photons absorbed in different regions of the solar spectrum for the three structures shown in figure 3. The infrared (IR) region (above the nc-Si band gap) is from 1.12 to 1.67 eV (1107 to 740 nm), the visible (Vis) region is from 1.67 to 3.1 eV (740 to 400 nm), and the ultraviolet (UV) region is from 3.1 to 4.43 eV (400 to 280 nm). The total absorption shown only includes the range above the nc-Si band gap energy from 1.12 to 4.43 eV (1100 to 280 nm). The IWP and WP structures have significantly improved performance in the IR region compared with the nc-Si thin film due to better light trapping. The photonic crystals both have a lower effective index of refraction such that reflection is decreased. The WP structure also has almost double the absorption of the thin film in the ultraviolet region due to better anti-reflection properties.

Table 2 lists the total solar absorption, A_{sol} (%), short-circuit current density J_{sc} (mA cm^{-2}), and the ultimate efficiency η (%) of these structures. The total solar absorption shown in this table is over the entire solar spectrum and not just over energies above the silicon band gap as shown in table 1. The solar absorption of the silicon thin film ideal single pass is 18.8%. The best IWP structure has a solar absorption of 33.3%, which is a 77.1% enhancement over the

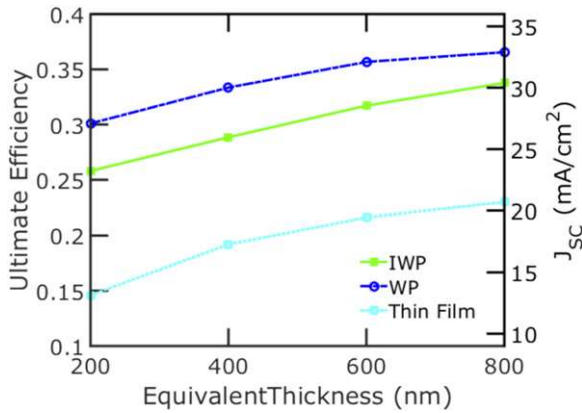


Figure 4. Ultimate efficiency of nc-Si IWP and WP photonic crystal structures and nc-Si thin film for various equivalent thicknesses. The corresponding short-circuit current density is shown on the right y-axis.

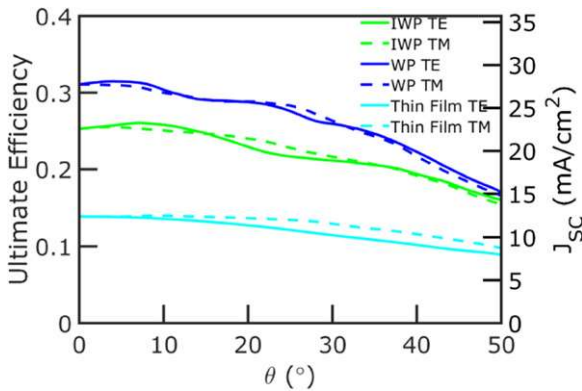


Figure 5. Solar absorption as a function of zenith angle θ for nc-Si IWP and WP photonic crystal structures and nc-Si thin film. The short-circuit current density is shown on the right y-axis.

thin-film structure. The absorption of the WP is 106% higher than that of the thin-film structure.

We further investigated IWP and WP photonic crystal structures of equivalent thicknesses, $L = 400, 600$ and 800 . The optimal ultimate efficiency of these two structures compared with thin films at various equivalent thicknesses is plotted in figure 4. The performance of the IWP and WP photonic crystal structures is generally better than that of nc-Si thin film over a wide range of equivalent thicknesses. The short-circuit current is shown on the right y-axis. The scatter plots of ultimate efficiency for IWP and WP photonic crystal structures with these equivalent thicknesses are shown in the Electronic Supplementary Material figure S1. Generally, the WP photonic crystal structures perform better over a wide range of diameters, pitches, and number of layers similar to when $L = 200$ nm as discussed before. In contrast, the performance of the IWP photonic crystal structures is much more sensitive to morphology.

Finally, we simulated the solar performance of the IWP, WP and thin-film structures for various angles of incidence θ from normal incidence to 50° . Figure 5 plots the ultimate efficiency of the various structures with equivalent thickness $L = 200$ nm for TE and TM polarized incident light. The

short-circuit current density is shown on the right y-axis. For the IWP and WP photonic crystal structures, the TE (TM) results are for the average of where the electric (magnetic) field is fixed along the x - and y -direction. There is little variation in absorption with the zenith angle up to about 40° . The TE and TM results exhibit very similar behavior.

3. Conclusion

In summary, we report that the solar absorption in nc-Si may be improved by structuring the active region into an IWP or WP crystal. The IWP and WP structures may be engineered such that there is a strong absorption enhancement in the infrared range, where the absorption is about 2.7 to 4.0 times that of a 200 nm equivalent thickness thin film, respectively. The IWP structure may be approximated as a thin film with an effective index of refraction where the absorption peaks correspond to TE and TM leaky modes in the film, whereas the WP structure exhibits absorption peaks corresponding to the coupling between TE and TM modes in the stacked cylinders. Generally, the WP structures exhibit improved performance compared to the IWP structures over a wide range of equivalent thicknesses and incidence angles. Future work will study how these structures may be scalably fabricated through the author Chen's interference lithography methods.

Acknowledgments

This work is supported by NSF Grant #1348591.

References

- [1] Feng N, Michel J, Zeng L, Liu J, Hong C Y, Kimerling L and Duan X 2007 *IEEE Trans. Electron Devices* **54** 1926–33
- [2] Kelzenberg M D, Boettcher S W, Petykiewicz J A, Turner-Evans D B, Putnam M C, Warren E L, Spurgeon J M, Briggs R M, Lewis N S and Atwater H A 2010 *Nat. Mater.* **9** 239–44
- [3] Garnett E and Yang P 2010 *Nano Lett.* **10** 1082–7
- [4] Peng K, Xu Y, Wu Y, Yan Y, Lee S T and Zhu J 2005 *Small* **1** 1062–7
- [5] Hu L and Chen G 2007 *Nano Lett.* **7** 3249–52
- [6] Lin Y, Harb A, Lozano K, Xu D and Chen K P 2009 *Opt. Express* **17** 16625–31
- [7] Wang B and Leu P W 2012 *Nanotechnology* **23** 194003
- [8] Jeong S, McGehee M D and Cui Y 2013 *Nat. Commun.* **4** 2950
- [9] Yoon J et al 2008 *Nat. Mater.* **7** 907–15
- [10] <http://redc.nrel.gov/solar/spectra/am1.5/>
- [11] Mallick S B, Agrawal M and Peumans P 2010 *Opt. Express* **18** 5691–706
- [12] Gao T, Stevens E, Lee J K and Leu P W 2014 *Opt. Lett.* **39** 4647–50
- [13] Pala R A, White J, Barnard E, Liu J and Brongersma M L 2009 *Adv. Mater.* **21** 3504–9 ISSN 09359648
- [14] Bernel P, Luo C, Zeng L, Kimerling L C and Joannopoulos J D 2007 *Opt. Express* **15** 16986–7000

- [15] Park Y, Drouard E, Daif O E, Letartre X, Viktorovitch P, Fave A, Kaminski A, Lemiti M and Seassal C 2009 *Opt. Express* **17** 14312–21
- [16] Tanaka Y, Kawamoto Y, Fujita M and Noda S 2013 *Opt. Express* **21** 20111–8
- [17] Lin Y, Rivera D and Chen K P 2006 *Opt. Express* **14** 887–92
- [18] Poole Z, Xu D, Chen K P, Olvera I, Ohlinger K and Lin Y 2007 *Appl. Phys. Lett.* **91** 251101
- [19] Lin Y, Harb A, Rodriguez D, Lozano K, Xu D and Chen K P 2008 *Opt. Express* **16** 9165–72
- [20] Shah A, Meier J, Vallat-Sauvain E, Wyrsh N, Kroll U, Droz C and Graf U 2003 *Sol. Energy Mater. Sol. Cells* **78** 469–91 critical review of amorphous and microcrystalline silicon materials and solar cells
- [21] Amans D, Callard S, Gagnaire A, Joseph J, Ledoux G and Huisken F 2003 *J. Appl. Phys.* **93** 4173–9
- [22] Wang B, Stevens E and Leu P W 2014 *Opt. Express* **22** A386–95
- [23] Berenger J P 1994 *J. Comput. Phys.* **114** 185–200
- [24] Tikhodeev S G, Yablonskii A L, Muljarov E A, Gippius N A and Ishihara T 2002 *Phys. Rev. B* **66** 045102
- [25] Cao L, White J S, Park J S, Schuller J A, Clemens B M and Brongersma M L 2009 *Nat. Mater.* **8** 643–7